Electronic Impurity Doping of a 2D Hybrid Lead Iodide Perovskite by Bi and Sn

Haipeng Lu,[1,2] Gabrielle Koknat,[3] Yi Yao,[3] Ji Hao,[1] Xixi Qin,[3] Chuanxiao Xiao,[1] Ruyi Song,[4] Florian Merz,[5] Markus Rampp,[6] Sebastian Kokott,[7] Christian Carbogno,[7] Tianyang Li,[3] Glenn Teeter,[1] Matthias Scheffler,[7] Joseph J. Berry,[1,8,9] David B. Mitzi,[3,4] Jeffrey L. Blackburn,[1] Volker Blum,[3,4,*] and Matthew C. Beard[1,8,†]

[1] *Material Chemical and Computational Science Directorate, National Renewable Energy Laboratory, Golden, Colorado 80401, USA*

[2] *Department of Chemistry, The Hong Kong University of Science and Technology, Clear Water Bay, Kowloon, Hong Kong SAR, China*

[3] *Thomas Lord Department of Mechanical Engineering and Material Science, Duke University, Durham, North Carolina 27708, USA*

[4] *Department of Chemistry, Duke University, Durham, North Carolina 27708, USA*

[5] *Lenovo HPC Innovation Center, Meitnerstr. 9, D-70563 Stuttgart, Germany*

[6] *Max Planck Computing and Data Facility, Giessenbachstrasse 2, D-85748 Garching, Germany*

[7] *The NOMAD Laboratory at the FHI of the Max-Planck-Gesellschaft and IRIS-Adlershof of the Humboldt-Universität zu Berlin, 14195 Berlin, Germany*

[8] *Renewable and Sustainable Energy Institute, University of Colorado Boulder, Boulder, Colorado 80309, USA*

[9] *Department of Physics, University of Colorado Boulder, Boulder, Colorado 80309, USA*

(Received 5 December 2022; revised 28 April 2023; accepted 4 May 2023; published 8 June 2023)

Control over conductivity and carrier type (electrons and holes) defines semiconductors. A primary approach to target carrier concentrations involves introducing a small population of aliovalent impurity dopant atoms. In a combined synthetic and computational study, we assess impurity doping by introducing Bi and Sn into the prototype 2D Ruddlesden-Popper hybrid perovskite phenylethylammonium lead iodide (PEA_2PbI_4). Experimentally, we demonstrate that Bi and Sn can achieve *n*- and *p*-type doping, respectively, but the doping efficiency is low. Simulations show that Bi introduces a deep defect energy level (∼0.5 eV below the conduction band minimum) that contributes to the low doping efficiency, but, to reproduce the low doping efficiency observed experimentally, an acceptor level must also be present that limits *n*-type doping. Experiments find that Sn achieves *p*-dopant behavior and simulations suggest that this occurs through the additional oxidation of Sn defects. We also study how substitutional Bi incorporation can be controlled by tuning the electrochemical environment during synthesis. First-principles impurity doping simulations can be challenging; typical dopant concentrations constitute less than 0.01% of the atoms, necessitating large supercells, while a high level of theory is needed to capture the electronic levels. We demonstrate simulations of complex defect-containing unit cells that include up to 3383 atoms, employing spin-orbit coupled hybrid density functional theory. While *p*- and *n*-type behavior can be achieved with Sn and Bi, simulations and experiments provide concrete directions where future efforts must be focused to achieve higher doping efficiency.

DOI: 10.1103/PRXEnergy.2.023010

*volker.blum@duke.edu
†Matt.Beard@nrel.gov

I. INTRODUCTION

Two-dimensional (2D) hybrid organic-inorganic metal-halide perovskites (MHPs) have recently emerged as promising semiconductors for solar cells, light-emitting diodes, opto-spintronics, and photodetectors [1–6]. Their rich chemical and structural tunability provides unique opportunities to control, for example, their structural distortion, quantum and dielectric confinement, exciton-phonon coupling, and Rashba splitting, which, in turn, modulate their optical, electronic, thermal, and spin properties. High crystalline quality, even for low-temperature solution-phase synthesis, adds to their promise. However, one significant drawback relates to the ability to precisely control their Fermi level, charge carrier densities, and majority carrier types [7,8]. In traditional inorganic semiconductors, efficient control of the carrier type and density is generally achieved by introducing impurity aliovalent atoms, i.e., dopants. In organic semiconductors, the carrier concentration and conductivity can be similarly tuned over many orders of magnitude by employing molecular dopants [9]. MHPs possess both organic and inorganic subcomponents and the variety of doping mechanisms are not fully understood, contributing to electronic doping that is much less efficient [8,10,11].

Past studies aimed at controlling doping in MHPs focused mostly on prototype 3D systems, $A\mathrm{Pb}X_3$ [$X = \mathrm{Cl}$, Br, I; $A = \mathrm{MA}$ (methylammonium), FA (formamidinium), Cs]. For example, aliovalent cations [12–15] such as Bi^{3+} increase the conductivity of $MAPbBr_3$ single crystals by 4 orders of magnitude, with an increase of *n*-type carrier concentration (from $\sim 10^9$ to $\sim 10^{11}$–10^{12} cm^{-3}) [12]. Bi^{3+}-doped $MAPbI_3$ single crystals also display resistivity that is reduced by 3 orders of magnitude compared to undoped single-crystal $MAPbI_3$ (from 10^8 to 10^5 Ω/cm) [16]. Interestingly, doping with isovalent ions (e.g., $Mg^{2+}, Sr^{2+}, Sn^{2+}$) [11,17,18] can also tune the $MAPbI_3$ Fermi level, with doping mechanisms that vary under different doping regimes (concentration) [11]. Computationally, substituting Bi for Pb is shown to form relatively deep defect levels in 3D MHPs, including $CsPbBr_3$, $CsPbCl_3$, $MAPbBr_3$, and $MAPbI_3$, for which predicted (+/0) transition levels range from 0.26 to 0.59 eV below the conduction band minimum (CBM) [8,19–25]. However, predictions for $FAPbI_3$ [19] and $CsPbI_3$ [20] indicate a much shallower dopant character, with (+/0) transition levels at 0.05 and 0.1 eV, respectively. In contrast, electronic doping in the 2D counterparts is understudied, although several reports have shown that impurity atoms (e.g., $Bi^{3+}, Mn^{2+}, Sn^{2+}$) [26–31] can be introduced into 2D MHPs to elicit interesting optical properties. For instance, Li *et al.* [31] showed that a small amount of isovalent Sn^{2+} dopants induced a broadband emission in phenylethylammonium lead iodide (PEA_2PbI_4) crystals, resulting from self-trapped excitons. Lyu *et al.* [26] demonstrated that Bi^{3+}-doped 2D BA_2PbI_4 crystals exhibited a new near-infrared (NIR) emission. However, electronic doping, i.e., modulation of carrier type, density, and Fermi level, has not been demonstrated in lead-based 2D MHPs.

Here, we experimentally and computationally study electronic doping of the prototype 2D Ruddlesden-Popper PEA_2PbI_4 with both aliovalent Bi^{3+} (*n*-type doping) and isovalent Sn^{2+} cations (*p*-type doping). Another doping strategy, not studied here, is to use molecular donors or acceptors intercalated into the organic layer [32] similar to studies at the surfaces of 3D $MAPbI_3$ [33,34]. The choice of PEA_2PbI_4 as a target is motivated by the fact that this system is the first 2D organic-inorganic MHP synthesized with a conjugated group (phenyl ring) [35], is widely studied, and the ability to successfully dope PEA_2PbI_4 would likely translate to the much broader class of other 2D MHPs. In our study, we find that both Bi^{3+} and Sn^{2+} can be substitutionally incorporated into PEA_2PbI_4 crystals, with drastically different incorporation efficiencies. Small amounts of incorporated Sn^{2+} or Bi^{3+} directly modulate the electronic structure, studied here with first-principles spin-orbit coupled hybrid density functional theory (DFT). This level of theory is computationally demanding but necessary to capture electronic band edge trends [36]. Importantly, our work overcomes a frequent drawback of such first-principles calculations for large complex semiconductor structures, namely, that calculations are typically limited to supercell models with a few hundreds of atoms, including all organic and inorganic components. Even when substituting just a single Pb^{2+} ion with an impurity in these limited supercells, the results are still closer to alloying (high impurity concentration) rather than to the dilute limit of impurity doping (low concentrations). Accordingly, the electronic levels induced by point defects in neighboring supercells of insufficient size can interact and may not capture the physicochemical properties of dilute impurity doping. Here, we demonstrate the computational enhancement of a high-precision all-electron hybrid DFT implementation in the electronic structure code FHI-AIMS [37–41], allowing the investigation of supercells with up to 3383 atoms to accurately capture the impurity limit in energy band structures. Our approach includes spin-orbit coupling [41] (SOC) and uses a single consistent density functional for both valence and core states, avoiding potential errors introduced by core-valence inconsistencies [42] (note that the static exchange term is the largest contribution to the core-valence error in Ref. [42]).

A key demonstration of the current study is the synergistic understanding of MHP doping that emerges from our simulations when coupled with targeted experiments. The simulations provide direct access to the energy of the defect level, a quantity that is difficult to access in experiments. Complementary experimental assessments, including conductivity measurements and

x-ray photoelectron spectroscopy (XPS) as a function of input impurity concentration, reveal the Fermi level modulation as a function of dopant incorporation. In combination, our results demonstrate electronic doping by Bi^{3+} and Sn^{2+} in PEA_2PbI_4 and provide a crucial insight into the underlying mechanisms. For isovalent Sn_{Pb} substitutions, our calculations support indirect doping by promoting Pb^{2+} vacancy formation in close proximity and forming a shallow acceptor level as one possible mechanism. For Bi_{Pb} substitutions, but likely also affecting other *n*-doping mechanisms, we identify a population of acceptors that currently limit the *n*-type doping efficiency in PEA_2PbI_4. To achieve greater control over the Fermi level, our results suggest that not only does Bi, perhaps the single most intuitive candidate *n*-dopant for a Pb-based semiconductor system, have too deep of a defect level but also that the doping efficiency is significantly hindered by these compensating acceptors. We find that the acceptors are independent of the Bi chemistry, and therefore, conclude that doping would be hindered, even with a dopant that has a shallower defect level, i.e., it would hinder any attempt at *n*-type doping. While we do not uncover here the chemical identity of the compensating defect, we can place limits on its characteristics and provide avenues towards understanding defects in future and ongoing work.

II. RESULTS AND DISCUSSION

A. Doping in PEA_2PbI_4 crystals

Single crystals of undoped, Bi^{3+}-doped, and Sn^{2+}-doped 2D PEA_2PbI_4 [Fig. 1(a)] are synthesized from a concentrated hydroiodic acid (HI) solution, containing hypophosphorous acid (H_3PO_2) as a reducing agent [43,44] (see Sec. IV). Small dopant equivalents are introduced by adding Bi_2O_3 or SnO_2 with different nominal ratios of Bi : Pb or Sn : Pb to the reaction mixture, while keeping the total metal content constant. Sn^{4+} is reduced to Sn^{2+} *in situ* by hypophosphorous acid; Bi^{3+} may also be reduced to Bi^{2+} (formally) when substitutionally incorporated for Pb^{2+}, facilitating *n*-type doping. In the following, we follow the convention of denoting doped samples as *x*% Bi or *x*% Sn, where *x*% corresponds to the atomic *input* ratio of Bi^{3+} or Sn^{2+} relative to Pb^{2+} in the feed solutions and not the incorporated impurity content.

The incorporation efficiency is studied by inductively coupled plasma mass spectrometry (ICPMS) [Fig. 1(b)]

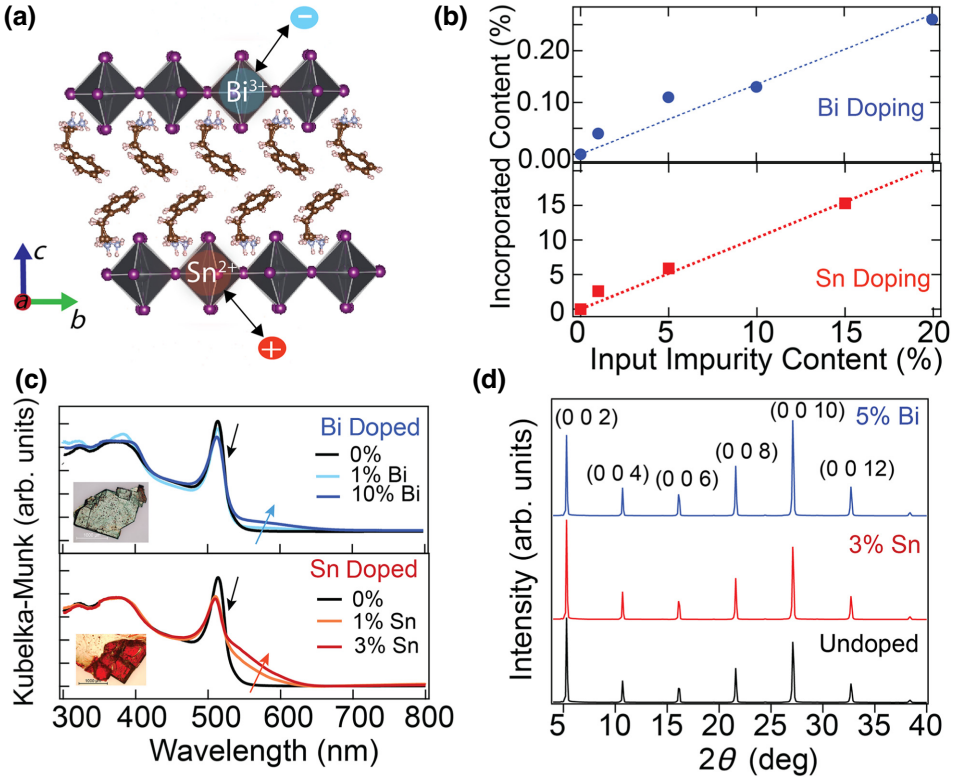

FIG. 1. (a) Crystal structure of PEA_2PbI_4 and illustrative doping effects by impurity atoms. (b) Summary of ICPMS data showing the ratio of incorporated dopants relative to Pb for input dopants Bi and Sn. Dotted lines indicate estimated linear approximations of the dopant incorporation levels as a guide to the eye. (c) UV-vis absorption spectra of undoped, Bi^{3+}-doped, and Sn^{2+}-doped PEA_2PbI_4. *x*% corresponds to the input atomic ratio of Bi^{3+} or Sn^{2+} relative to Pb^{2+}; inset shows optical images of as-grown doped crystals. (d) PXRD spectra of undoped, 5% Bi^{3+}-doped, and 3% Sn^{2+}-doped PEA_2PbI_4 crystals.

and is 0.013 ± 0.002 and 1.03 ± 0.02 for Bi^{3+} and Sn^{2+}, respectively [errors are from best fits of lines to data in Fig. 1(b)], indicating 100 times higher incorporation efficiency of Sn^{2+} compared with Bi^{3+}, which is consistent with the low interexchange energy of Pb^{2+} and Sn^{2+} [45]. An incorporation efficiency greater than one could be associated with a concomitant increase in Pb vacancies. As the dopant concentration increases, the color of Bi^{3+}-doped PEA_2PbI_4 crystals gradually changes from orange to dark red and eventually to black [inset, Fig. 1(c)], while that of Sn^{2+}-doped PEA_2PbI_4 crystals changes from orange to deep red [inset, Fig. 1(c)], suggesting a significant effect on the electronic structure.

Linear optical properties of powders are measured by diffuse reflectance spectroscopy, and absorption spectra are obtained using the Kubelka-Munk equation: $\alpha/S = (1-R)^2/(2R)$, where α is the absorption coefficient, S is the scattering coefficient, and R is the absolute reflectance [Fig. 1(c)]. Despite the striking color change clearly observed upon Bi^{3+} or Sn^{2+} incorporation, the absorption spectra of doped PEA_2PbI_4 mostly reproduce that of undoped PEA_2PbI_4 with an exciton peak at 514 nm. When normalized at the higher energy bands (300–450 nm), we find that the exciton peak absorption is slightly quenched, suggesting the presence of excess delocalized electrons or holes that partially block exciton transitions. This excitonic quenching results from the phase-space filling effect, which has been discussed extensively for other excitonic semiconductors [46–48]. An additional absorption tail at longer wavelengths apparently accounts for the color change. In contrast to Bi^{3+}, even 1% input Sn changes the absorption spectra significantly, confirming a higher incorporation efficiency for Sn^{2+} compared with Bi^{3+}. It is worth noting that the absorption tails associated with Bi^{3+} versus Sn^{2+} may arise for different underlying reasons. We tentatively associate the tail of Bi^{3+}, which has a low incorporation efficiency, with the defect states that it introduces (see Sec. II D below). In contrast, Sn^{2+} has a much higher incorporation efficiency and the overall reduction of the band gap by Sn^{2+} incorporation may be responsible for the tail. A similar tail appears, e.g., in the layered perovskite $(R\text{-MBA})_2Pb_{1-x}Sn_xI_4$ [R-MBA = (R)-methylbenzylammonium] at Sn input levels $x = 0.05$ and was tentatively attributed to areas of locally higher Sn^{2+} concentration and associated lower band gaps due to inhomogeneous Sn distribution [44].

Powder x-ray diffraction (PXRD) patterns of undoped, 5% Bi^{3+}-doped, and 3% Sn^{2+}-doped PEA_2PbI_4 crystals all show the same patterns [i.e., (00l) peaks, Fig. 1(d)], indicating no significant impact on the crystal structure when incorporating dopant atoms. The observed peaks represent the interlayer distance between inorganic Pb-I sheets, which is mostly defined by the organic cations and remains unchanged. While the space group of the undoped PEA_2PbI_4 crystals is refined to centrosymmetric P-1, we find that the 3% Bi^{3+}-doped crystals can be refined to either centrosymmetric P-1 or noncentrosymmetric Cc space groups (Table S4.1 within the Supplemental Material [49]). This effect is similar to that found previously for single-crystal XRD of Sn^{2+}-doped crystals, which reveals a change of the space group [31], suggesting successful Bi^{3+} incorporation.

B. Computational approach: Doping effects of Sn^{2+} and Bi^{3+} in PEA_2PbI_4 crystals

We perform first-principles calculations based on spin-orbit coupled hybrid DFT [41]. The screened-exchange HSE06 density functional [41,42] is used with standard parameters [exchange mixing 0.25, screening parameter 0.11 (Bohr radii)$^{-1}$] [50]. The present choice qualitatively captures energy band alignments in Pb-based layered MHPs and quantitatively underestimates their band gaps by a few tenths of eV [51–53]. This underestimation falls into the general range of prediction errors of this parameterization of the HSE06 density functional for semiconductors in this band gap range [54]. Thus, the HSE06 parametrization used here is expected to be appropriate for the present Pb- and Bi-containing metal-halide perovskites. We optimize the existing implementation [39] of hybrid DFT in the high-precision all-electron electronic structure code, FHI-AIMS [37–41], allowing up to 3383 atom supercells to be modeled. Fully relaxed atomic structures (lattice parameters and atomic positions) obtained at the level of dispersion-corrected semilocal DFT [PBE functional [55], including the Tkatchenko-Scheffler (TS) correction [56]] are used for the underlying geometries. This level of theory yields atomic structures in close agreement with experimental structures for other organic-inorganic hybrids (see Table S4.2 within the Supplemental Material [49] for a comparison of experimental and computational lattice parameters of different organic-inorganic hybrids at this level of theory; deviations are typically well below 2%) [6,44,49,51,52,57–64].

For the calculation of defect energy levels, we use generalized Kohn-Sham eigenvalue differences derived from the HSE06 + SOC functional, based on the observation that this nonlocal density functional comes close to satisfying the generalized Koopman theorem (GKT), as outlined in more detail in Ref. [65]. With this approach, we are able to avoid the introduction of supercell calculations with an explicit artificial background charge and associated charge corrections [66–68] that would be required when employing total-energy differences of charged supercells. The calculated supercells in this work are all electrically neutral. The applicability of the GKT essentially relies on the fact that differences between occupied defect levels and unoccupied band edges take on the role of the fundamental gap in defect-free systems. For predictions of the fundamental gap, the qualitative accuracy of the HSE06 + SOC

functional for the prediction of band gaps of semiconductors has been established in numerous references over the years [50,52,54,69]. We note that including SOC is critical, since it can shift energy bands associated with the Pb and Bi 6*p* electron derived conduction bands by about 1 eV relative to one another (see Refs. [41,50,51] and Fig. S2.15 within the Supplemental Material [49]) Our computational predictions qualitatively agree with energy levels derived from a model of the observed Fermi level shift with Bi incorporated concentration in PEA_2PbI_4, which also reveals the likely presence of a set of deeper-lying intrinsic defect states (see Secs. II D and II H), further validating our approach.

C. Incorporation mechanism of Sn^{2+}

According to previous observations [31], isovalent Sn^{2+} undergoes substitutional doping, replacing Pb^{2+}. A 1504-atom structure with a substitution of 1 in 32 Pb atoms by Sn, as shown in Figs. 2(a) and 2(b) and referred to as (4×4)-Sn_{Pb}, is simulated [Fig. 2(c)]. This supercell models a substitution of 3% of Pb atoms by Sn. In interpreting this value, it is important to note that the overall number of atoms in the supercell is much larger than just the number of Pb sites. The Sn incorporation corresponds to a substitution of less than 0.07% of atoms overall. At this limit, Sn incorporation slightly reduces the band gap to 1.95 eV, compared with 2.01 eV in the pristine structure, consistent with previous observations [70–72]. With increasing Sn content (Figs. S1.9–S1.11 within the Supplemental Material [49]), the band gap narrows further (Figs. S2.9–S2.11 and S3.8–S3.10 within the Supplemental Material [49]). A largely halide-derived state with contributions from the Sn^{2+} *s* states forms at the top of the valence band [17,18]. However, already at the limit of Fig. 2(c), the associated band is not energetically separated from Pb-I states (given only ∼60 meV difference between the 1.95 eV band gap and the pristine case). A visualization of this topmost Sn-derived valence orbital at the Γ point [yellow

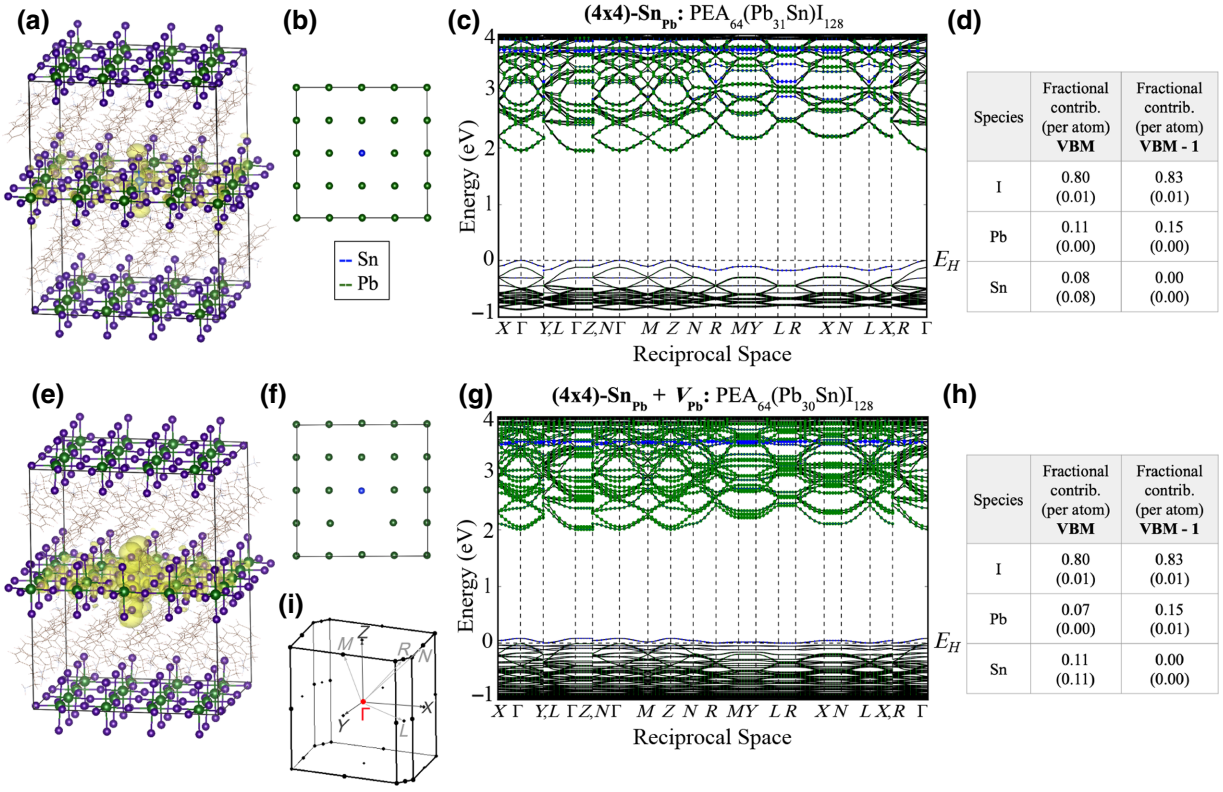

Species	Fractional contrib. (per atom) **VBM**	Fractional contrib. (per atom) **VBM - 1**
I	0.80 (0.01)	0.83 (0.01)
Pb	0.11 (0.00)	0.15 (0.00)
Sn	0.08 (0.08)	0.00 (0.00)

Species	Fractional contrib. (per atom) **VBM**	Fractional contrib. (per atom) **VBM - 1**
I	0.80 (0.01)	0.83 (0.01)
Pb	0.07 (0.00)	0.15 (0.01)
Sn	0.11 (0.11)	0.00 (0.00)

FIG. 2. (4×4)-Sn_{Pb} and (4×4)-$Sn_{Pb} + V_{Pb}$ structural models. (a) Full geometry of (4×4)-Sn_{Pb}; Pb in green, Sn in blue (atom in center), I in purple; wire models indicate PEA molecules. The orbital associated with the highest occupied Sn_{Pb}-derived state at the Γ point is shown by the yellow isosurface (of isosurface level 0.03, corresponding to $|\Psi|$), showing that this is an extended state, essentially hybridized with the host (PEA_2PbI_4) valence band. (b) Defect-containing layer of (4×4)-Sn_{Pb}, showing only the *B*-site atoms (Pb or Sn) for clarity. (c) Computed DFT-HSE06 + SOC electronic band structure of (4×4)-Sn_{Pb}, Brillouin zone definition shown in (i). Contribution of *B*-site atoms to different bands; Pb is green and Sn is blue. Species contributions of Sn (blue) are layered on top of contributions from Pb (green). The dashed black horizontal line labeled E_H indicates the energy above which states are unoccupied in the computation. (Note that this is not a Fermi level, since the calculations do not include a formal temperature.) (d) Tabulated fractions of species contributions to the VBM and the electronic state directly below the VBM (VBM-1) at the Γ point. Values are listed as total fractions and (in brackets) fractions per atom. Note the high Sn contribution (per atom) to the VBM. Analogous results are given for the (4×4)-$Sn_{Pb} + V_{Pb}$ structure in (e)–(h).

isosurface in Fig. 2(a)] indicates significant delocalization, consistent with hybridization with Pb^{2+} states. Overall, this scenario is closer to the formation of an alloy than to that of a traditional dopant state, even for the large (4×4) defect arrangement. Sn^{2+} does not itself provide an acceptor state; however, it is known that oxidation of the Sn-derived state can introduce holes [17,18]. This oxidation-assisted *p*-doping is the likely active mechanism in the experimental samples reported here as well.

We validate the hypothesis of oxidation-driven *p*-doping from Sn by direct calculations shown in Figs. 2(e)–2(h) (and Figs. S1.12–S1.15 and S2.12–S2.14 within the Supplemental Material [49]), using a nearby Pb^{2+} vacancy as a plausible oxidizing agent. Specifically, the placement of the Pb^{2+} vacancy directly next to a Sn^{2+} dopant results in a shallow unoccupied level just above the valence band maximum (VBM) that is nevertheless separated (by a few meV) from the remaining states [Fig. 2(g)]. Formally, this state may be understood as the oxidation of Sn^{II} to Sn^{IV} to provide two otherwise missing electrons to the I^- anions adjacent to the Pb^{2+} vacancy. Indeed, the isosurface density plot [Fig. 2(e)] shows that this state is largely localized at the I^- anions near the Sn_{Pb} substitution and the adjacent Pb^{2+} vacancy. The now-empty level is the Sn-enriched level that is the highest occupied level in the vacancy-free structure, as shown by Mulliken population analyses of these states in Figs. 2(d) and 2(h). For comparison, Figs. S1.15 and S2.14 within the Supplemental Material [49] show a structural model and band structures for a supercell with a Pb^{2+} vacancy and a Sn_{Pb} substitution placed in different inorganic layers, i.e., far away from one another. In this case, the empty state associated with the I^- anions near the Pb^{2+} vacancy is not energetically separated from the remaining valence states. Also, the DFT-PBE + TS total energy indicates that the formation of the Pb^{2+} vacancy is energetically favorable by about 0.3 eV if the vacancy is located next to the Sn_{Pb} defect, rather than far away from it. This energy difference provides a possible driving force for a *p*-type doping enhancement in the presence of Sn.

D. Incorporation mechanism of Bi^{3+}

The incorporation of aliovalent Bi^{3+} could be accompanied by the formation of a compensating Pb^{2+} vacancy. We consider two plausible mechanisms. The first is substitutional doping, namely, every Bi^{3+} ion directly substitutes a Pb^{2+} ion, requiring an extra electron to formally reduce Bi^{3+} to Bi^{2+} to balance the charge in the crystal, referred to as reduced mechanism (1). When the extra electron associated with Bi^{2+} is ionized, *n*-type electronic doping results. In the unreduced mechanism (2), two Bi^{3+} ions substitute for three Pb^{2+} ions, generating a compensating *B*-site vacancy to balance the charge. Here, no weakly bound electrons or holes will be generated, and thus no electronic doping will result.

Reduced mechanism:

$$PEA_2PbI_4 + x\,Bi^{3+} + x\,e^- \rightarrow PEA_2(Pb_{1-x}Bi_x)I_4 + x Pb^{2+}. \quad (1)$$

Unreduced mechanism:

$$PEA_2PbI_4 + 2x/3\,Bi^{3+} \rightarrow PEA_2(Pb_{1-x}Bi_{2x/3}\square_{x/3})I_4 + x\,Pb^{2+}. \quad (2)$$

Here, x denotes a fractional number quantifying Bi incorporation and $\square$ denotes a structural vacancy at the Pb^{2+} site.

Schematic models of corresponding Bi dopant incorporation models in (4×4) arrangements with respect to the underlying *B*-site atom positions (either Pb or Bi) are shown in Fig. 3(b). Reduction-type doping, mechanism (1), is modeled through a 1504-atom model, (4×4)-Bi_{Pb}, in which one Pb^{2+} (out of 32) is replaced by one Bi^{3+} (reduced to Bi^{2+}, in a spin-polarized calculation to account for the unpaired e^- situated at the Bi site). Again, in terms of the full structure, this model corresponds to substituting less than 0.07% of atoms overall. Nonreduction type doping, mechanism (2), is simulated through a 1503-atom model, (4×4)-$Bi_2\square$, in which three Pb^{2+} are replaced by two Bi^{3+} and a vacancy. In the (4×4)-$Bi_2\square$ model, the vacancy is placed near both Bi substituents, to satisfy the local charge balance. Both modes of Bi^{3+} incorporation introduce defect states that are close to, but well separated from, the conduction band edge [Figs. 3(c) and 3(d)], reducing the electronic band gap, and thus, offering a possible explanation for the experimentally observed low-energy tail of the UV-vis absorption spectrum.

The undoped PEA_2PbI_4 band gap value is 2.01 eV (Figs. S2.1 and S2.2 within the Supplemental Material [49]), while the highest occupied defect state in the substitutionally doped (4×4)-Bi_{Pb} structure is approximately 1.47 eV above the VBM. Thus, the position of the Bi_{Pb}-induced defect states is about 0.5 eV below the CBM, consistent with computational predictions of similarly Bi-derived defect states in 3D metal-halide perovskites [18–24]. The defect states in (4×4)-$Bi_2\square$ are unoccupied and situated somewhat higher, around 1.76 eV above the VBM, i.e., about 0.25 eV below the CBM. Figures 3(e) and 3(f) visualize the DFT-HSE06 + SOC orbitals associated with Bi dopants in (4×4)-Bi_{Pb} and (4×4)-$Bi_2\square$ arrangements in PEA_2PbI_4. In line with the essentially flat defect band, the defect state associated with substitutional Bi^{2+} is localized within the (4×4) arrangement, indicating an electron bound to Bi^{3+} at $T = 0$. Likewise, the defect state associated with the $Bi_2\square$ defect is well localized; however, *it does not contain electrons* but could act as an acceptor for any free electrons, i.e., its formation would be detrimental to *n*-type doping.

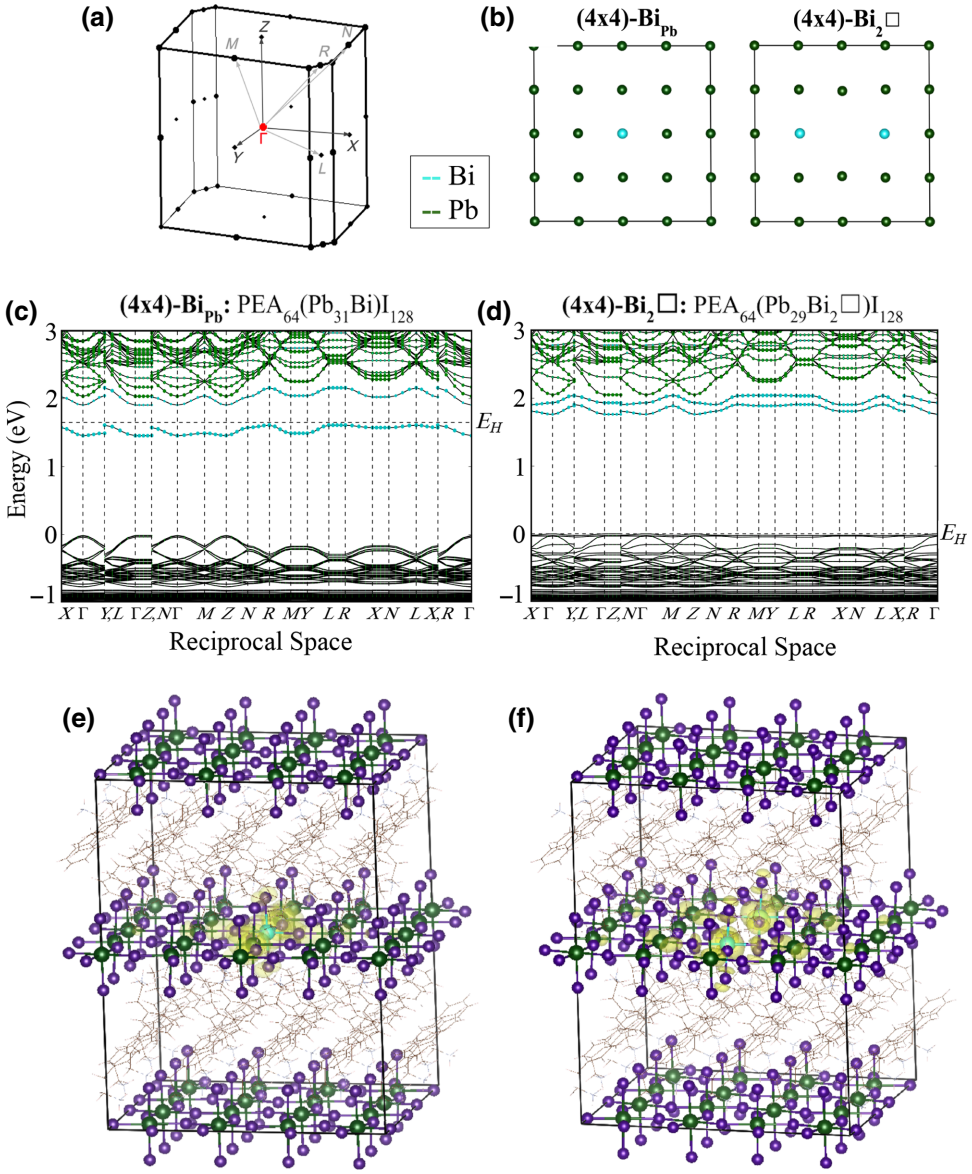

FIG. 3. Structural models, DFT-HSE06 + SOC predicted band structures, and orbitals for the reduced and nonreduced Bi-incorporated structures (4 × 4)-Bi_{Pb} and (4 × 4)-Bi_2□, respectively (see text). (a) Brillouin zone. (b) Impurity-containing layers of the substitutional defect and the vacancy-forming defect models, showing only *B*-site positions—Pb (green), Bi (cyan), or vacancy—for clarity. Computed DFT-HSE06 + SOC electronic band structures of (c) substitutionally doped (4 × 4)-Bi_{Pb} (spin-polarized) and (d) vacancy structure (4 × 4)-Bi_2□. Bands highlighted in green are predominantly derived from Pb; bands highlighted in cyan are predominantly derived from Bi. Highest occupied level in (c) is the band around 1.5 eV. (e) Orbital associated with the occupied Bi-derived defect band at the Γ point of (4 × 4)-Bi_{Pb} shown for an isosurface value (corresponding to $|\Psi|$) of 0.03. (f) Analogous to (e), but for (4 × 4)-Bi_2□. Pb, green; Bi, cyan; I, purple; wireframe, PEA. Dashed black horizontal lines labeled E_H in (c),(d) indicate the energy above which states are unoccupied in the computation. (Note that this is not a Fermi level, since the calculations do not include a formal temperature.)

These trends are not apparent from smaller models comprising 188, 376, and 751 atoms, respectively, each featuring a single Bi_{Pb} or Bi_2□ defect (see Figs. S1.3 –S1.5, S2.3 –S2.5, and S3.3 –S3.5 within the Supplemental Material [49]). Smaller structural models result in larger overlap between orbitals of the neighboring atoms, which results in larger dispersion of the energetic states, as illustrated in the band structure figures. This overlap obfuscates electron location, therefore, making conclusions about occupation more elusive. Importantly, in Figs. 3(c) and 3(d), the electronic levels associated with Bi defects in adjacent supercells appear to be essentially decoupled from one another (indicated by the largely flat bands). While the ratio of Bi impurities to Pb sites in the model (3%)

is still a factor of 30 higher than the incorporated impurity content seen in Fig. 1(b), the electronic characteristics of an isolated Bi_{Pb} defect are captured by the 1504-atom supercell and would no longer change substantially even if the supercell size were increased further. For the $Bi_2\square$ defect, Fig. 3(d) still shows some residual dispersion in the empty states associated with Bi^{3+}, consistent with the fact that the two Bi sites are only separated by one Pb site (and associated halide anions), as seen in Fig. 3(f). However, the $Bi_2\square$-derived states in a smaller 751-atom (2×4) model (Figs. S1.5 and S2.5 within the Supplemental Material [49]) are much more dispersive than their counterparts in the (4×4) model [Fig. 3(d)], showing that it essentially approaches the dilute limit of the $Bi_2\square$ defect. To unambiguously clarify the nature of the empty $Bi_2\square$ defect bands as localized flat bands that are well separated from the PEA_2PbI_4 conduction bands, we additionally include a band structure calculation of a 3383-atom (6×6) arrangement of $Bi_2\square$ defects (Fig. S2.8 within the Supplemental Material [49]) using DFT-HSE06 + SOC and intermediate settings of FHI-AIMS. As expected, the Bi-derived states become essentially completely flat and retain their character as unoccupied defect states that are close to, but clearly separated from, the PEA_2PbI_4 host conduction bands. The unusually demanding computational cell of >3000 atoms used here allows us to unambiguously demonstrate the nature of the Bi^{2+}-derived orbitals as localized dopant-like states that are cleanly separated from the energy bands associated with the PEA_2PbI_4 host system.

E. Chemical nature of impurity doping

To estimate whether mechanism (1) or (2) is more favorable, we compare DFT-derived formation energies of substitutional versus vacancy-forming defects. As written, Eqs. (1) and (2) are incomplete, since they lack anions and/or electron sources that are determined by the synthetic environment. In our specific case, we can substitute with specific compounds present during synthesis as follows. This substitution changes Eq. (1) into

$$PEA_2PbI_4 + x/2\ Bi_2O_3 + x/2\ H_3PO_2 \xrightarrow[+xe^-]{+xe^-} PEA_2(Pb_{1-x}Bi_x)I_4 + x\,PbO + x/2\ H_3PO_3; \tag{3}$$

this substitution changes Eq. (2) into

$$PEA_2PbI_4 + x/3\ Bi_2O_3 \rightarrow PEA_2(Pb_{1-x}\,Bi_{2x/3}\,\square_{x/3})I_4 + x\,PbO. \tag{4}$$

The key difference is that reaction pathways (1) and (3) require an electron source, whereas (2) and (4) do not depend on the chemical potential of electrons, i.e., on reducing versus oxidizing conditions. In Eq. (3), we explicitly show that electrons must transfer to Bi^{3+} from H_3PO_2, forming Bi^{2+} and H_3PO_3, while in Eq. (4) the formal oxidation state of Bi remains the same. To illustrate the impact of the range of possible experimental conditions, we consider two alternative electron-providing half-reactions that, while not expected in our synthetic environment, could hypothetically serve as electron sources:

$$O^{2-} + H_2 \rightarrow H_2O + 2e^-, \tag{5}$$

$$O^{2-} \rightarrow 1/2\,O_2 + 2e^-. \tag{6}$$

In Table I, we summarize the defect formation energies at the level of DFT-PBE + TS, for reaction pathways (3), (1) + (5), (1) + (6), and (4). We compare energies for different supercell models, up to the largest, (4×4) defect models. Pathway (4) does not depend on the presence or absence of a reducing agent and leads to a high positive formation energy of about 2 eV. In contrast, the formation energy for the reducing mechanism depends on the electron source. For H_3PO_2 or H_2, a defect formation energy (per Bi atom) of about 0.7–0.8 eV results, while assuming O_2 formation from O^{2-} as the only available reservoir leads to less favorable conditions (2.4 eV).

The results (Table I) are qualitative in nature: they assume specific reagents, rely on gas-phase computed total energies, and do not account for concentrations and/or partial pressures. Nevertheless, the calculated defect incorporation energies illustrate our key point, which is that the environment employed when incorporating electronic dopants during synthesis can determine whether a reduced form (no compensating vacancies) or oxidized form (with compensating vacancies) of a particular dopant is incorporated. Our synthesis includes a reducing agent, H_3PO_2, thus we expect that Bi is predominantly incorporated as a substitutional dopant without forming compensating vacancies. In contrast to Bi, the formation energies computed for Sn incorporation and using our experimental reagents are always favorable (see Tables S10.2 and S10.4 within the Supplemental Material [49],

TABLE I. Computed defect formation energies of different Bi-incorporation mechanisms, i.e., for H_2, O_2, and H_3PO_2 considered as electron sources. Defect energies are given per defect, i.e., per single Bi_{Pb} substitution and per single $Bi_2\square$ composite defect. See Sec. I within the Supplemental Material for an overview of the models employed. Values given for (4×4)-Bi_{Pb} are calculated for the spin-polarized system, where the spin-polarized total energy is calculated using intermediate settings in FHI-AIMS. See Tables S10.1 and S10.3 within the Supplemental Material [49] for reaction equations and total-energy values.

ΔE_{defect}	Electron source	$(c2\times2)$-Bi_{Pb}: $PEA_8(Pb_3Bi)I_{16}$	(2×2)-Bi_{Pb}: $PEA_{16}(Pb_7Bi)I_{32}$	(2×4)-$Bi_2\square$: $PEA_{32}(Pb_{13}Bi_2\square)I_{64}$	(4×4)-Bi_{Pb}: $PEA_{64}(Pb_{31}Bi)I_{128}$	(4×4)-$Bi_2\square$: $PEA_{64}(Pb_{29}Bi_2\square)I_{128}$
Formation energy (eV)	none			2.076		1.957
	H_2	0.682	0.618		0.762	
	O_2	2.296	2.231		2.375	
	H_3PO_2	0.626	0.561		0.705	

consistent with the experimental conclusion that essentially all available Sn is incorporated into the synthesized crystals. The calculated formation energies per incorporated Sn atom for different Sn-impurity structures are as follows: 3%-impurity structure, (4×4)-Sn_{Pb}, –0.233 eV/Sn; 50% alloyed, $c(2\times2)$-Sn_{Pb}, –0.233 eV/Sn; fully substituted structure, $(c2\times2)$-Sn_{Pb}, –0.240 eV. The calculated energy values per Sn atom do not vary appreciably with Sn concentration, consistent with the idea that a substitutional alloy without strong Sn-Sn attraction or repulsion forms.

F. Impurity doping in PEA_2PbI_4 thin films

When single crystals of undoped, Bi^{3+}-doped, and Sn^{2+}-doped PEA_2PbI_4 are dissolved in DMF and spin-cast onto quartz substrates, they do not display changes to their crystal structures or any changes in preferred film orientation of the doped versus undoped films (XRD, Fig. S5.1 within the Supplemental Material [49]). UV-vis analysis exhibits similar behavior to that of the powder samples, i.e., quenched exciton absorption and an absorption tail below the exciton transition [Fig. S6.1(a) within the Supplemental Material [49]]. The films also exhibit quenched photoluminescence (PL) [Fig. S6.1(b) within the Supplemental Material [49]], with the degree of PL quenching strongly related to the incorporated dopant concentration, i.e., more dopants result in larger PL quenching. Time-resolved photoluminescence (TRPL) measurements indicate that the PL lifetime (∼1.1-ns monoexponential decay) remains essentially the same for Bi and Sn incorporation; this is likely due to low incorporated metal concentrations [Fig. S6.1(c) within the Supplemental Material [49]].

High-resolution (HR) XPS shows the presence of both Sn^{2+} and Sn^{4+} in 3% Sn-doped films (Fig. S7.1 within the Supplemental Material [49]) consistent with partial oxidation of Sn^{2+} to Sn^{4+}, while the Bi-incorporated content is too low to detect by XPS. Scanning electron microscopy (SEM) images show very similar morphology and roughness for the undoped and doped films, and energy-dispersive x-ray spectroscopy (EDX) reveals a homogeneous distribution of Sn and Bi (submicron resolution) with no obvious dopant segregation (Fig. S8.1 within the Supplemental Material [49]). Thus, evidence that the Sn and Bi impurities incorporated into crystals are also incorporated into films is obtained from the optoelectrical measurements, so we assume that the amount incorporated in the films is proportional to that in the crystals.

G. Electronic doping in PEA_2PbI_4 thin films

All PEA_2PbI_4 thin films are measured with air-free methods to eliminate any impact of external oxidation during their characterization. Four-point probe sheet resistance measurements are obtained by averaging values from five different random spots, with resistivities in the 10^{10} Ω/sq range. As the Sn or Bi dopant concentration increases, the sheet resistance decreases and then gradually plateaus [Fig. 4(a)]. 3% Sn-doped and 20% Bi-doped PEA_2PbI_4 thin films display 30% and 50% reduction in sheet resistance, respectively, suggesting an increased population of delocalized electrons and holes.

Concurrently, HRXPS analysis of the valence band edge region [Figs. 4(b) and 4(c)] exhibits a shift of the valence band maximum (E_{VBM}) with respect to the Fermi level (E_F) upon doping (note that in XPS data the Fermi level is the reference energy and is set to zero). While we appreciate that the XPS probes mostly the surface region of the films, we assume that the bulk Fermi level tracks the surface Fermi level. $E_F - E_{VBM}$ for the undoped PEA_2PbI_4 film is 1.49 eV. Assuming the band gap (E_g) equals the sum of the exciton energy (514 nm or 2.41 eV) and the exciton binding energy (0.26 eV) [73], i.e., $E_g = 2.41 + 0.26 = 2.67$ eV [53], undoped PEA_2PbI_4 is slightly *n*-type. Bi^{3+} dopants shift E_{VBM} further from E_F, indicating more *n*-type behavior, with a shift as large as 440 meV that levels off at higher Bi input, similar to the trend in resistance. On the other hand, when Sn^{2+} is added, E_{VBM} shifts closer to E_F, indicating a more *p*-type film. The Fermi level shift is as large as about 200 meV in 3% Sn-doped PEA_2PbI_4. The resistance measurements and XPS data demonstrate that incorporated Bi^{3+} dopants

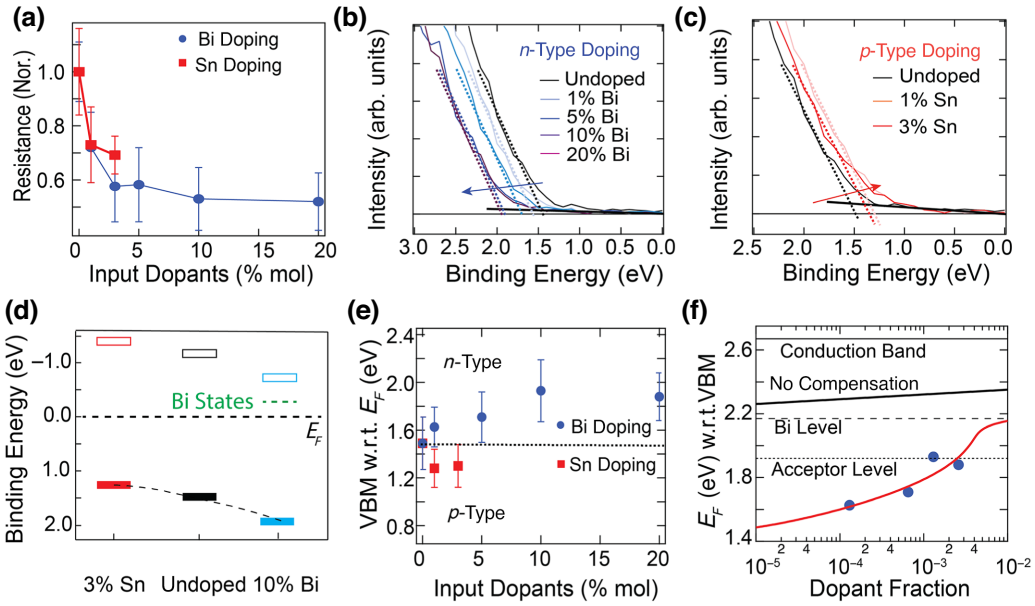

FIG. 4. (a) Sheet resistance of PEA_2PbI_4 films versus dopant concentration. (b),(c) HRXPS spectra of the valence band edge region as a function of dopant concentration for Bi and Sn, respectively. (d) E_{VBM} with respect to E_F ($E_F - E_{VBM}$) as a function of dopant concentration; CBM is plotted as unfilled rectangles and is determined as the VBM plus the electronic band gap, taken here to be 2.67 eV. (e) Extracted band edge energies of undoped, Sn-doped, and Bi-doped PEA_2PbI_4 films with respect to the Fermi level (set to zero here). To extract E_{VBM} with respect to E_F ($E_F - E_{VBM}$), a linear fit of the photoelectron intensity onset is performed, and the intersection with the baseline is extracted. (f) Fermi level with respect to VBM (VBM is set to zero here) as a function of incorporated Bi dopant fraction. Blue dots, experimental data extracted from XPS results. Red line, model including a compensating trap level (Sec. XI within the Supplemental Material [49]). Black solid line, model without compensation.

introduce delocalized electrons, while Sn^{2+} dopants induce delocalized holes.

H. Electronic doping mechanism in PEA_2PbI_4

Our data demonstrate that we can achieve both *n*- and *p*-type electronic impurity doping through incorporating Bi and Sn, respectively. Figure 4(d) plots the extracted VBM (filled rectangles) as a function of input dopant concentration, where the CBM (unfilled rectangles) is calculated by adding the electronic band gap to the XPS-determined VBM. However, neither case results in a large increase to the conductivity or Fermi level. As noted above, the question of the mechanism of *p*-type doping through isovalent Sn_{Pb} substitution is complicated by the fact that isovalent substitution of Pb(II) by Sn(II) should not itself lead to *p*-doping, since Sn(II) itself does not introduce acceptor levels, according to chemical intuition and our extensive DFT simulations. Indirect doping, through rendering the formation of V_{Pb} more favorable in close proximity to Sn_{Pb}, can account for the *p*-type doping observed experimentally. In fact, such a mechanism should be relatively inefficient (also in agreement with our experiments) due to the overall still low (but nonzero) probability of V_{Pb} formation. Alternatively, surface oxidation of Sn(II) species by residual oxidizing agents, such as O_2, could be another mechanism to account for the formation of holes in Sn(II)-containing MHPs [17]. In our experiments, these processes are relatively inefficient, as evidenced by a Fermi level shift of only 220 meV at the surface of the doped film. In contrast, while the dopant incorporation is much smaller with Bi doping, the Fermi level shift is 2 times larger, indicating a much higher doping efficiency for Bi compared with Sn, i.e., more delocalized carriers are introduced per dopant atom incorporation.

The *n*-type doping in 2D PEA_2PbI_4 by Bi^{3+} can be understood by direct substitutional doping mechanism (1). However, the shift in the Fermi level observed is smaller than what is expected for an impurity dopant, even with a deep-defect level of 0.5 eV below the conduction band. To illustrate, we plot the expected shift in Fermi level as a function of the fraction of dopant incorporation, $f_d = N_d/N_0$ [black solid line, Fig. 4(f)], where N_d is the density of incorporated Bi defects and N_0 is the overall Pb density. A full derivation of the underlying physical model is provided in Sec. XI within the Supplemental Material [49]. There are two characteristic features for which measured data [blue circles in Fig. 4(f), extracted from Fig. 4(e) by setting the VBM to zero] do not agree with the prediction; (1) the initial Fermi level shift is too small, and (2) the subsequent shift in Fermi level position with increasing doping is larger than expected. In the case of

normal doping, the Fermi level position over the range of f_d values from 10^{-5} to 10^{-2} should vary from 2.25 to 2.35 eV (Fig. 4(f), black solid line) and would correspond to a doping efficiency of $\eta = n_{el}/N_d$, where n_{el} is the dopant-induced electron density, which is around 10^{-2} and decreases with increasing dopant incorporation (Fig. S11.4 within the Supplemental Material [49]). However, our results suggest that the actual doping efficiency must be much lower (Fig. 4(f), blue circles), i.e., the measured Fermi level varies only from 1.5 to 1.9 eV with f_d varying between 10^{-4} and 10^{-2}. A model with a single dopant level, even if very deep (i.e., when $E_d = 1.5$ eV), cannot explain these features, as shown in Fig. S11.1 within the Supplemental Material [49].

We therefore consider an alternative model that includes a fixed concentration of electron acceptors that are able to capture ionized electrons arising from the Bi dopant atoms [49,74]. Our model can reproduce the observed shifts in Fermi level position [red trace in Fig. 4(f)] when the fraction, $f_a = N_a/N_0$, where N_a is the density of electron acceptors, is about 10^{-3} and the acceptor level is about 0.7–0.8 eV below the CBM [dotted line in Fig. 4(f)]. Figs. S11.2 and S11.3 within the Supplemental Material [49] further substantiate the specific acceptor level, about 0.7–0.8 eV, and density, about 10^{-3}, showing that substantially different values cannot reproduce our measured data similarly well. It is the consistency between the computationally derived defect level for Bi, the XPS-derived Fermi level shifts, and the observed changes in resistivity that lead us to consider the presence of this deeper acceptor population as the most likely culprit limiting our effort to electronically dope $(PEA)_2PbI_4$ with Bi. We also simulate the case where every incorporated Bi dopant produces a compensating defect, i.e., the concentration of compensating defects varies with input Bi dopant concentration; however, this cannot reproduce our measurements. In fact, such behavior would result in a completely pinned Fermi level (see Fig. S11.5 within the Supplemental Material [49]), which is clearly not observed here. Thus, we conclude that most of the Bi electrons are captured by a fixed concentration of acceptors, compensating for the Bi dopant electrons.

There are several possible defects that could serve as the compensating acceptors. While, in principle, the unreduced Bi defect, i.e., reaction mechanism (2), would produce an empty state that could accept electrons at about 0.25 eV below the conduction band, we rule this out because (1) in our simulations, the acceptor states must be lower than about 0.7 eV to reproduce our data; (2) the calculated formation energy would suggest that the concentration of these defects would be too low to explain our data; and (3) we simulate the case where the acceptor level concentration varies with the impurity concentration and find that this cannot explain the experimental observations (Fig. S11.5 within the Supplemental Material [49]). For 3D $MAPbI_3$, Nazeeruddin *et al.* [75] identified two point defects that accepted electrons and were likely associated with iodine and MA. Similar point defects may also form in the 2D case and could be responsible for the observations reported here. Another potential source of an electron acceptor could be a tightly bound polaron. Li *et al.* found that small impurity dopants in 2D $n = 1$ PEA_2PbI_4 could induce a self-trapped exciton that was about 0.7 eV below the band edge [31]. However, we can rule out a tightly bound polaron [76] as being responsible for the lower than expected doping efficiency, since that will have the same statistics as a varying concentration of compensating defects, and we found that imposing such a constrait cannot reproduce our results. A tightly bound polaron should also lead to a lower effective defect level (i.e., lower than the computational value), but that also cannot explain our experimental results.

In future work, it would be valuable to subject the intrinsic and Bi-induced extrinsic defect landscape to a systematic computational search that resolves the detailed nature of the compensating defect revealed in our work. We stress, however, that such an investigation is not simple due to the enormous structural freedom afforded by the relatively open 2D PEA_2PbI_4 structure and large unit cell. Regarding Bi doping, the success of the present work is to (1) experimentally quantify the extent of attainable *n*-type doping by Bi incorporation; (2) quantify the approximate depth of the Bi donor level by detailed and rather demanding high-level theory; and (3) demonstrate that no single defect state can explain the observed degree of *n* doping, revealing the existence of a compensating defect level.

III. CONCLUSION

We systematically study electronic doping of the prototype 2D perovskite PEA_2PbI_4 by using isovalent Sn^{2+} and aliovalent Bi^{3+} in both crystals and thin films. Four-point probe measurements and XPS data indicate that both Sn^{2+} and Bi^{3+} can moderately tune the carrier type and concentration, with Sn^{2+} as a *p*-type dopant and Bi^{3+} as an *n*-type dopant. We combine experimental observations with first-principles DFT simulations of defect-containing supercell models, including up to 3383 atoms to study impurity doping with high-level methods (spin-orbit coupled hybrid DFT). We find that both Sn and Bi dopants induce a slightly quenched exciton transition and a lower-energy absorption tail, and DFT calculations confirm that Sn dopants decrease the band gap of PEA_2PbI_4, while Bi dopants introduce defect states. Consistent with our calculations, Sn and Bi dopants do not appear to dramatically change the crystal structure of PEA_2PbI_4. We show that substituting Pb^{2+} by Sn^{2+} is favorable, and the incorporation efficiency of Sn^{2+} is nearly 100%, indicating that the subsequent reaction to yield delocalized holes limits

electronic doping. We show that the formation of V_{Pb} defects in close proximity to substituted Sn_{Pb} is one plausible doping mechanism that would introduce more V_{Pb} vacancies and would lead to a shallow acceptor defect state. However, in the case of Bi^{3+} dopants, we observe two doping characteristics that differ from Sn^{2+}. First, Bi^{3+} incorporation is about 10 times smaller than that of 3D $MAPbI_3$ (incorporation efficiency of 0.18 in $MAPbI_3$; Fig. S9.1 within the Supplemental Material [49,77]). Second, the Bi doping efficiency, η (number of electrons introduced per incorporated dopant atom), while much higher than for Sn doping, is lower in the 2D than the 3D case. We hypothesize that these issues could be associated with the more ionic and flexible lattice of 2D perovskites, which promotes the formation of various defects, including metal vacancies, iodide vacancies, and interstitial iodide defects, making the aliovalent Bi^{3+} electronic doping less efficient. We find that for *n*-type doping the doping efficiency is limited by a population of acceptors. These compensating acceptors must be identified and avoided to fully unpin the Fermi level in 2D perovskites.

IV. METHODS

A. General methods

All sample preparations are performed using standard air-free techniques on a Schlenk line under a nitrogen atmosphere or in a nitrogen-filled glovebox.

B. Materials

All chemicals are used as received, unless otherwise indicated. Lead oxide (PbO, 99.999%), bismuth(III) oxide (Bi_2O_3, 99.999%), PEA (≥99%), *N*,*N*-anhydrous DMF, 57% w/w aqueous HI solution (99.95%, distilled, and stabilized by H_3PO_2), and 50% w/w aqueous hypophosphorous acid solution are purchased from Sigma-Aldrich. Tin(IV) oxide (SnO_2, 99.9%) is purchased from Alfa-Aesar, and it is ground using a mortar and pestle before use.

C. Synthesis of $(PEA)_2PbI_4$ single crystals

2D perovskite $(PEA)_2PbI_4$ single crystals are synthesized based on a previously reported cooling method [5]. Briefly, 200 mg (0.90 mmol) of PbO and 200 µl (1.59 mmol) of PEA are fully dissolved in 4 ml of HI and 0.5 ml of H_3PO_2 solution at 90 °C. The solution is then slowly cooled to room temperature at a rate of 2 °C/h, giving orange sheetlike crystals. The crystals are then isolated from the parent solution by vacuum filtration, washed with a small amount of diethyl ether, and dried under vacuum.

D. Synthesis of Bi-doped $(PEA)_2PbI_4$ single crystals

Bi-doped 2D perovskite $(PEA)_2PbI_4$ single crystals are synthesized by introducing a small amount of Bi_2O_3 into the reaction mixture mentioned in Sec. IV C. Briefly, PbO and Bi_2O_3 with different nominal ratios (Bi:Pb ratios of 0.01, 0.03, 0.05, 0.1, and 0.2, with a total [PbO + Bi_2O_3] amount of 0.90 mmol) and 200 µl (1.59 mmol) of PEA are fully dissolved at 90 °C in a solution containing 4 ml of HI solution and 0.5 ml of H_3PO_2. The solution is then slowly cooled to room temperature at a rate of 2 °C/h, giving dark-red to black sheetlike crystals. The crystals are then isolated from the parent solution by vacuum filtration, washed with a small amount of diethyl ether, and dried under vacuum.

E. Synthesis of Sn-doped $(PEA)_2PbI_4$ single crystals.

Sn-doped 2D perovskite $(PEA)_2PbI_4$ single crystals are synthesized by introducing a small amount of SnO_2 into the reaction mixture mentioned in Sec. IV C. Generally, PbO and SnO_2 with different nominal ratios (Sn:Pb ratios of 0.01, 0.03, 0.05, and 0.15, with a total [PbO + SnO_2] amount of 0.90 mmol) and 200 µl (1.59 mmol) of PEA are fully dissolved at 90 °C in a solution containing 4 ml of HI solution and 0.5 ml of H_3PO_2. The solution is then slowly cooled to room temperature at a rate of 2 °C/h, giving red sheetlike crystals. The crystals are then isolated from the parent solution by vacuum filtration, washed with a small amount of diethyl ether, and dried under vacuum.

F. Preparation of undoped, Bi^{3+}-doped, and Sn^{2+}-doped $(PEA)_2PbI_4$ thin films

Quartz or FTO substrates are washed sequentially using acetone and isopropanol in a sonicator for 10 min each, followed by an ultraviolet-ozone treatment for 15 min. Precursor solutions are prepared by dissolving the corresponding crystals in DMF at 10 wt% (e.g., 20 mg in 200 µl) and are immediately used. Thin films are prepared in a N_2-filled glovebox by spin coating the precursor solution onto substrates using a spin rate of 4000 rpm for 30 s, followed by thermal annealing at 100 °C for 10 min. Thin films on quartz substrates are used for UV-vis, PL, TRPL, and XRD measurements. Thin films on FTO are used for XPS, UPS, SEM, and EDX measurements.

G. Powder and single-crystal x-ray diffraction

Powder x-ray diffraction measurements are collected on a Rigaku DMax 2200 diffractometer with a rotating Cu anode. Single-crystal diffraction data are collected on a Bruker D8 ADVANCE series II instrument at 293 K using Mo $K\alpha$ radiation ($\lambda = 0.71073$ Å). For the powder x-ray diffraction, small peaks, other than the marked (002*l*) peaks (Fig. S5.1 within the Supplemental Material) [49], are due to tungsten contamination of the Cu anode, which generates an additional x-ray radiation wavelength of 1.47 Å [78]. For the single crystal diffraction experiments, a full sphere of diffraction data is collected and multiscan empirical absorption correction is applied. Structure solution is

obtained by direct methods using the SHELXS program and refined using the least-squares method by employing the SHELXL [79] program within the Olex2 software [80].

H. Optical absorption measurements

For powder absorption, powder samples are first obtained by grinding single crystals using a mortar and pestle. Linear optical absorption spectra are obtained by performing optical diffuse reflectance measurements in a Cary 5000 UV-vis-NIR spectrometer operating in the 300–800 nm range at room temperature. A $BaSO_4$ pellet is used as the reference for 100% reflectance, and $BaSO_4$ powder is also used to dilute powder samples for all measurements. Linear optical absorption spectra of powders are generated by converting reflectance into absorption data using the Kubelka-Munk equation [81]: $\alpha/S = (1-R)^2/(2R)$, where R is the reflectance and α and S are the absorption and scattering coefficients, respectively. For thin-film absorption, absorption spectra are collected in transmission mode using a quartz substrate as the reference for 100% transmittance.

I. SEM and EDX measurements

SEM and EDS images are collected on a Hitachi 4800 SEM platform. SEM mapping is done at an electron beam condition of 3 kV and 2 μA, while EDS mapping is done at an electron beam condition of 20 kV and 5 μA for higher signal intensity.

J. XPS measurements

XPS measurements are acquired on a Physical Electronics Phi 5600 instrument. Samples were transferred using air-free methods. HRXPS spectra are acquired using monochromatic Al $K\alpha$ x-rays ($h\nu = 1486.7$ eV), with a pass energy of 23.5 eV.

K. Four-point probe measurements

Four-point probe measurements are performed by using a Signatone four-point resistance system with a self-developed LabVIEW program. All measurements are conducted on thin films (on glass substrates) under dark conditions inside the nitrogen-filled glovebox. A Keithley source and meter are employed to source the voltage and measure the current. For each sample, current-voltage curves are measured and recorded for at least five different positions on each sample, and the sheet resistance is calculated and averaged from the slope of the I-V curves.

L. First-principles calculations

The FHI-AIMS all-electron electronic structure software package is used to perform first-principles DFT calculations [37–41]. FHI-AIMS is capable of computing the properties of large and complex systems, enabling the semilocal and spin-orbit coupled hybrid DFT calculations reported in this work. The hybrid DFT implementation of Ref. [39] is optimized in detail for this work. Besides loop level optimizations to improve the single core performance, the memory consumption and communication overhead within a compute node is reduced significantly by introducing shared-memory features, standardized in version 3 of the message passing interface (MPI) standard, into the code. On the multinode scale, the MPI communication patterns and load balancing are improved significantly to allow for efficient calculations on current massively parallel computing architectures. Specifically, the Intel Skylake processor-based supercomputers Stampede2 (Texas Advanced Computing Center at the University of Texas at Austin through the XSEDE infrastructure) and Eagle at the National Renewable Energy Laboratory are used for this work, employing several thousand CPU cores simultaneously for the largest computations reported here. We furthermore use the Max-Planck Computing and Data Facility's Raven supercomputer. Exemplary timings are reported for one specific simulation [Figs. 2(e)–2(h)] in Table S12.1 within the Supplemental Material [49]. Technical details of the overall improved hybrid DFT implementation in the FHI-AIMS code will be reported in a separate publication. Table S12.1 within the Supplemental Material [49] includes tabulated values for resources used in the (4×4)-$Sn_{Pb} + V_{Pb}$ calculations. The Perdew-Berke-Ernzerhof (PBE) [55] density functional plus the TS correction [56] for van der Waals interactions is used to optimize the atomic coordinates and lattice parameters of each investigated structure model to reflect minima of the Born-Oppenheimer potential energy surface. "Tight" FHI-AIMS numerical default settings are used for relaxations. Past work on hybrid organic-inorganic perovskites showed that this overall approach yielded computational structure predictions in close agreement with experimental structures for organic-inorganic hybrid metal-halide semiconductors [6,44,51,52].

The Heyd-Scuseria-Ernzerhof (HSE06) hybrid density functional [82,83], with a screening parameter of 0.11 (bohr radii)$^{-1}$, an exchange mixing parameter of 0.25, and non-self-consistent spin-orbit coupling (SOC) [41], is used for calculations of band structure properties and orbital visualizations [41,82,83]. See Fig. S2.15 within the Supplemental Material [49] for the impact of SOC on electronic structure results for the doped system. "Intermediate" FHI-AIMS default settings are used for band structure and orbital calculations. A Gaussian broadening function of narrow width, w, is used to determine orbital occupations close to the boundary between unoccupied states (the FHI-AIMS defaults are $w = 0.01$ eV for systems with an appreciable gap or $w = 0.05$ eV for systems with a gap smaller than 0.2 eV between occupied and unoccupied states in the calculation). Gamma-centered $(n_1 \times n_2 \times n_3)$ k-point grids are chosen to be sufficiently dense by

ensuring the products of n_i and lattice vector length $|a_i|$ are at least 40 Å in length, where $|a_i|$ is the length of the ith real-space unit vector ($i = 1,2,3$) and n_i is an integer in reciprocal space. A $(2 \times 2 \times 2)$ k-point grid is used to relax the (4×4)-Sn_{Pb}, (4×4)-Bi_{Pb}, and (4×4)-$Bi_2\square$ structures. A $(3 \times 3 \times 3)$ k-point grid is used to calculate the electronic structures of the (4×4) models. Additional k-point grids for the relaxations and electronic structure calculations of the smaller impurity models are included in the Supplemental Material [49].

Data that support the findings in this paper can be found in the Supplemental Material [49]. The very large geometry files for the 1500-atom calculations are not included in the Supplemental Material [49] due to their size. These files, and all other FHI-AIMS input and output files, can be found in the NOMAD repository; individual digital object identifier URLs are provided in the Supplemental Material [49] for each atomic structure model considered in this paper. Any additional data can be obtained through correspondence with the authors upon reasonable request.

ACKNOWLEDGMENTS

This work was primarily supported as part of the Center for Hybrid Organic Inorganic Semiconductors for Energy (CHOISE) an Energy Frontier Research Center funded by the Office of Basic Energy Sciences, Office of Science within the U.S. Department of Energy. Part of this work was authored by the Alliance for Sustainable Energy, LLC, the manager and operator of the National Renewable Energy Laboratory for DOE under Contract No. DE-AC36-08GO28308. The views expressed in the article do not necessarily represent the views of the DOE or the U.S. Government. Initial density functional calculations and data analysis by G.K. were supported by the National Science Foundation under Grants No. 1709294 and No. 1729297. Calculations and data analysis by G.K. on combined Sn substitution/vacancy defects were supported by the U.S. Department of Energy, Office of Science, Office of Workforce Development for Teachers and Scientists, Office of Science Graduate Student Research (SCGSR) program. The SCGSR program is administered by the Oak Ridge Institute for Science and Education for the DOE under Contract No. DE-SC0014664. Y.Y. acknowledges funding support through the National Science Foundation under Grant No. 1450280. D.B.M. and T.L. acknowledge funding support through the National Science Foundation under Grant No. 2004869. This work used the Extreme Science and Engineering Discovery Environment (XSEDE), which is supported by National Science Foundation Grant No. ACI-1548562. Specifically, the work used the Stampede2 computer at the Texas Advanced Computing Center through Allocation No. TG-DMR200077. Computer simulations were also carried out using resources of the National Energy Research Scientific Computing Center (NERSC), a U.S. Department of Energy (DOE) Office of Science User Facility operated under Contract No. DE-AC02-05CH11231. A portion of the research was performed using computational resources sponsored by the Department of Energy's Office of Energy Efficiency and Renewable Energy and located at the National Renewable Energy Laboratory. The hybrid DFT development work received funding from the European Union's Horizon 2020 Research and Innovation Programme (grant agreement No. 951786, the NOMAD CoE), and the ERC Advanced Grant TEC1P (No. 740233).

H.L. and G.K. contributed equally to this work.

The authors declare no competing financial interest.

[1] F. Zhang, H. Lu, J. Tong, J. J. Berry, M. C. Beard, and K. Zhu, Advances in two-dimensional organic–inorganic hybrid perovskites, Energy Environ. Sci. **13**, 1154 (2020).

[2] L. Mao, C. C. Stoumpos, and M. G. Kanatzidis, Two-dimensional hybrid halide perovskites: Principles and promises, J. Am. Chem. Soc. **141**, 1171 (2019).

[3] I. C. Smith, E. T. Hoke, D. Solis-Ibarra, M. D. McGehee, and H. I. Karunadasa, A layered hybrid perovskite solar-cell absorber with enhanced moisture stability, Angew. Chem., Int. Ed. **53**, 11232 (2014).

[4] L. Pedesseau, D. Sapori, B. Traore, R. Robles, H.-H. Fang, M. A. Loi, H. Tsai, W. Nie, J.-C. Blancon, A. Neukirch, S. Tretiak, A. D. Mohite, C. Katan, J. Even, and M. Kepenekian, Advances and promises of layered halide hybrid perovskite semiconductors, ACS Nano **10**, 9776 (2016).

[5] H. Lu, J. Wang, C. Xiao, X. Pan, X. Chen, R. Brunecky, J. J. Berry, K. Zhu, M. C. Beard, and Z. V. Vardeny, Spin-dependent charge transport through 2D chiral hybrid lead-iodide perovskites, Sci. Adv. **5**, eaay0571 (2019).

[6] M. K. Jana, R. Song, H. Liu, D. R. Khanal, S. M. Janke, R. Zhao, C. Liu, Z. V. Vardeny, V. Blum, and D. B. Mitzi, Organic-to-inorganic structural chirality transfer in a 2D hybrid perovskite and impact on Rashba-Dresselhaus spin-orbit coupling, Nat. Commun. **11**, 4699 (2020).

[7] E. Amerling, H. Lu, B. W. Larson, A. E. Maughan, A. Phillips, E. Lafalce, L. Whittaker-Brooks, J. J. Berry, M. C. Beard, Z. Valy Vardeny, and J. L. Blackburn, A multi-dimensional perspective on electronic doping in metal halide perovskites, ACS Energy Lett. **6**, 1104 (2021).

[8] J. Euvrard, Y. Yan, and D. B. Mitzi, Electrical doping in halide perovskites, Nat. Rev. Mater. **6**, 531 (2021).

[9] I. Salzmann, G. Heimel, M. Oehzelt, S. Winkler, and N. Koch, Molecular electrical doping of organic semiconductors: Fundamental mechanisms and emerging dopant design rules, Acc. Chem. Res. **49**, 370 (2016).

[10] Y. Zhou, J. Chen, O. M. Bakr, and H.-T. Sun, Metal-doped lead halide perovskites: Synthesis, properties, and optoelectronic applications, Chem. Mater. **30**, 6589 (2018).

[11] N. Phung, R. Félix, D. Meggiolaro, A. Al-Ashouri, G. S. Silva, C. Hartmann, J. Hidalgo, H. Köbler, E. Mosconi, B. Lai *et al.*, The doping mechanism of halide perovskite

unveiled by alkaline earth metals, J. Am. Chem. Soc. **142**, 2364 (2020).

[12] A. L. Abdelhady, M. I. Saidaminov, B. Murali, V. Adinolfi, O. Voznyy, K. Katsiev, E. Alarousu, R. Comin, I. Dursun, L. Sinatra, E. H. Sargent, O. F. Mohammed, and O. M. Bakr, Heterovalent dopant incorporation for bandgap and type engineering of perovskite crystals, J. Phys. Chem. Lett. **7**, 295 (2016).

[13] M. Liu, G. Zhong, Y. Yin, J. Miao, K. Li, C. Wang, X. Xu, C. Shen, and H. Meng, Aluminum-doped cesium lead bromide perovskite nanocrystals with stable blue photoluminescence used for display backlight, Adv. Sci. **4**, 1700335 (2017).

[14] G. Pan, X. Bai, D. Yang, X. Chen, P. Jing, S. Qu, L. Zhang, D. Zhou, J. Zhu, W. Xu, B. Dong, and H. Song, Doping lanthanide into perovskite nanocrystals: Highly improved and expanded optical properties, Nano Lett. **17**, 8005 (2017).

[15] D. Zhou, D. Liu, G. Pan, X. Chen, D. Li, W. Xu, X. Bai, and H. Song, Cerium and ytterbium codoped halide perovskite quantum dots: A novel and efficient downconverter for improving the performance of silicon solar cells, Adv. Mater. **29**, 1704149 (2017).

[16] C. Li, X. Chen, N. Li, J. Liu, B. Yuan, Y. Li, M. Wang, F. Xu, Y. Wu, and B. Cao, Highly conductive *n*-type $CH_3NH_3PbI_3$ single crystals doped with bismuth donors, J. Mater. Chem. C **8**, 3694 (2020).

[17] D. Ricciarelli, D. Meggiolaro, F. Ambrosio, and F. De Angelis, Instability of tin iodide perovskites: Bulk *p*-doping versus surface tin oxidation, ACS Energy Lett. **5**, 2787 (2020).

[18] D. Meggiolaro, D. Ricciarelli, A. A. Alasmari, F. A. S. Alasmary, and F. De Angelis, Tin versus lead redox chemistry modulates charge trapping and self-doping in tin/lead iodide perovskites, J. Phys. Chem. Lett. **11**, 3546 (2020).

[19] J. L. Lyons, Effective donor dopants for lead halide perovskites, Chem. Mater. **33**, 6200 (2021).

[20] Y. Kang, S. Kang, and S. Han, Influence of Bi doping on physical properties of lead halide perovskites: a comparative first-principles study between $CsPbI_3$ and $CsPbBr_3$, Mater. Today Adv. **3**, 100019 (2019).

[21] Z.-L. Yu, Y.-Q. Zhao, Q. Wan, B. Liu, J.-L. Yang, and M.-Q. Cai, Theoretical study on the effect of the optical properties and electronic structure for the Bi-doped $CsPbBr_3$, J. Phys.: Condens. Matter **32**, 205504 (2020).

[22] J. Yin, G. H. Ahmed, O. M. Bakr, J.-L. Brédas, and O. F. Mohammed, Unlocking the effect of trivalent metal doping in all-inorganic $CsPbBr_3$ perovskite, ACS Energy Lett. **4**, 789 (2019).

[23] E. Mosconi, B. Merabet, D. Meggiolaro, A. Zaoui, and F. De Angelis, First-principles modeling of bismuth doping in the $MAPbI_3$ perovskite, J. Phys. Chem. C **122**, 14107 (2018).

[24] X. Zhang, J.-X. Shen, M. E. Turiansky, and C. G. Van de Walle, Hidden role of Bi incorporation in nonradiative recombination in methylammonium lead iodide, J. Mater. Chem. A **8**, 12964 (2020).

[25] M. Pizzochero, G. B. Barin, K. n. Čerņevičs, S. Wang, P. Ruffieux, R. Fasel, and O. V. Yazyev, Edge disorder in bottom-up zigzag graphene nanoribbons: Implications for magnetism and quantum electronic transport, J. Phys. Chem. Lett. **12**, 4692 (2021).

[26] F. Lyu, X. Zheng, Y. Wang, R. Shi, J. Yang, Z. Li, J. Yu, and B.-L. Lin, Bi^{3+} doped 2D Ruddlesden–Popper organic lead halide perovskites, J. Mater. Chem. A **7**, 15627 (2019).

[27] D. Cortecchia, W. Mróz, S. Neutzner, T. Borzda, G. Folpini, R. Brescia, and A. Petrozza, Defect engineering in 2D perovskite by Mn(II) doping for light-emitting applications, Chem **5**, 2146 (2019).

[28] L. Zhang, T. Jiang, C. Yi, J. Wu, X.-K. Liu, Y. He, Y. Miao, Y. Zhang, H. Zhang, X. Xie, P. Wang, R. Li, F. Gao, W. Huang, and J. Wang, Bright free exciton electroluminescence from Mn-doped two-dimensional layered perovskites, J. Phys. Chem. Lett. **10**, 3171 (2019).

[29] Q. Ba, A. Jana, L. Wang, and K. S. Kim, Dual emission of water-stable 2D organic–inorganic halide perovskites with Mn(II) dopant, Adv. Funct. Mater. **29**, 1904768 (2019).

[30] A. Biswas, R. Bakthavatsalam, and J. Kundu, Efficient exciton to dopant energy transfer in Mn^{2+}-doped $(C_4H_9NH_3)_2PbBr_4$ two-dimensional (2D) layered perovskites, Chem. Mater. **29**, 7816 (2017).

[31] T. Li, X. Chen, X. Wang, H. Lu, Y. Yan, M. C. Beard, and D. B. Mitzi, Origin of broad-band emission and impact of structural dimensionality in tin-alloyed Ruddlesden–Popper hybrid lead iodide perovskites, ACS Energy Lett. **5**, 347 (2020).

[32] J. V. Passarelli, C. M. Mauck, S. W. Winslow, C. F. Perkinson, J. C. Bard, H. Sai, K. W. Williams, A. Narayanan, D. J. Fairfield, M. P. Hendricks *et al.*, Tunable exciton binding energy in 2D hybrid layered perovskites through donor–acceptor interactions within the organic layer, Nat. Chem. **12**, 672 (2020).

[33] Q. Jiang, Z. Ni, G. Xu, Y. Lin, P. N. Rudd, R. Xue, Y. Li, Y. Li, Y. Gao, and J. Huang, Interfacial molecular doping of metal halide perovskites for highly efficient solar cells, Adv. Mater. **32**, 2001581 (2020).

[34] J. Euvrard, O. Gunawan, X. Zhong, S. P. Harvey, A. Kahn, and D. B. Mitzi, *p*-Type molecular doping by charge transfer in halide perovskite, Mater. Adv. **2**, 2956 (2021).

[35] J. Calabrese, N. L. Jones, R. L. Harlow, N. Herron, D. L. Thorn, and Y. Wang, Preparation and characterization of layered lead halide compounds, J. Am. Chem. Soc. **113**, 2328 (1991).

[36] J. P. Perdew, W. Yang, K. Burke, Z. Yang, E. K. U. Gross, M. Scheffler, G. E. Scuseria, T. M. Henderson, I. Y. Ying Zhang, A. Ruzsinszky *et al.*, Understanding band gaps of solids in generalized Kohn–Sham theory, Proc. Natl. Acad. Sci. U. S. A. **114**, 2801 (2017).

[37] V. Blum, R. Gehrke, F. Hanke, P. Havu, V. Havu, X. Ren, K. Reuter, and M. Scheffler, *Ab initio* molecular simulations with numeric atom-centered orbitals, Comput. Phys. Commun. **180**, 2175 (2009).

[38] V. Havu, V. Blum, P. Havu, and M. Scheffler, Efficient O(N) integration for all-electron electronic structure calculation using numeric basis functions, J. Comput. Phys. **228**, 8367 (2009).

[39] S. V. Levchenko, X. Ren, J. Wieferink, R. Johanni, P. Rinke, V. Blum, and M. Scheffler, Hybrid functionals for large periodic systems in an all-electron, numeric atom-centered basis framework, Comput. Phys. Commun. **192**, 60 (2015).

[40] F. Knuth, C. Carbogno, V. Atalla, V. Blum, and M. Scheffler, All-electron formalism for total energy strain

derivatives and stress tensor components for numeric atom-centered orbitals, Comput. Phys. Commun. **190**, 33 (2015).

[41] W. P. Huhn and V. Blum, One-hundred-three compound band-structure benchmark of post-self-consistent spin-orbit coupling treatments in density functional theory, Phys. Rev. Mater. **1**, 033803 (2017).

[42] R. Gómez-Abal, X. Li, M. Scheffler, and C. Ambrosch-Draxl, Influence of the Core-Valence Interaction and of the Pseudopotential Approximation on the Electron Self-Energy in Semiconductors, Phys. Rev. Lett. **101**, 106404 (2008).

[43] X. Chen, H. Lu, Z. Li, Y. Zhai, P. F. Ndione, J. J. Berry, K. Zhu, Y. Yang, and M. C. Beard, Impact of layer thickness on the charge carrier and spin coherence lifetime in two-dimensional layered perovskite single crystals, ACS Energy Lett. **3**, 2273 (2018).

[44] H. Lu, C. Xiao, R. Song, T. Li, A. E. Maughan, A. Levin, R. Brunecky, J. J. Berry, D. B. Mitzi, V. Blum, and M. C. Beard, Highly distorted chiral two-dimensional tin iodide perovskites for spin polarized charge transport, J. Am. Chem. Soc. **142**, 13030 (2020).

[45] G. E. Eperon and D. S. Ginger, *B*-Site metal cation exchange in halide perovskites, ACS Energy Lett. **2**, 1190 (2017).

[46] D. M. Kroupa, B. K. Hughes, E. M. Miller, D. T. Moore, N. C. Anderson, B. D. Chernomordik, A. J. Nozik, and M. C. Beard, Synthesis and spectroscopy of silver-doped PbSe quantum dots, J. Am. Chem. Soc. **139**, 10382 (2017).

[47] H. Lu, G. M. Carroll, X. Chen, D. K. Amarasinghe, N. R. Neale, E. M. Miller, P. C. Sercel, F. A. Rabuffetti, A. L. Efros, and M. C. Beard, *n*-Type PbSe quantum dots via post-synthetic indium doping, J. Am. Chem. Soc. **140**, 13753 (2018).

[48] J. L. Blackburn, A. J. Ferguson, and O. G. Reid, *Handbook of Carbon Nanomaterials* (World Scientific, Singapore, 2019), pp. 237.

[49] See the Supplemental Material at http://link.aps.org/supplemental/10.1103/PRXEnergy.2.023010 for the geometries, band structures, and densities of states used in electronic structure simulations; XRD data and crystal structure refinement of Bi-doped PEA_2PbI_4; photophysical characterization, XPS, SEM, and EDX data for Bi- and Sn-doped PEA_2PbI_4 thin films; comparison of Bi^{3+} doping efficiency for 3D $MAPbI_3$ and 2D PEA_2PbI_4; reaction equations and total energies used to compute defect formation energies; model of Fermi level position as a function of dopant incorporation without and with consideration of compensating defects; and indicative computational resources.

[50] A. V. Krukau, O. A. Vydrov, A. F. Izmaylov, and G. E. Scuseria, Influence of the exchange screening parameter on the performance of screened hybrid functionals, J. Chem. Phys. **125**, 224106 (2006).

[51] M. K. Jana, S. M. Janke, D. J. Dirkes, S. Dovletgeldi, C. Liu, X. Qin, K. Gundogdu, W. You, V. Blum, and D. B. Mitzi, Direct-bandgap 2D silver–bismuth iodide double perovskite: The structure-directing influence of an oligothiophene spacer cation, J. Am. Chem. Soc. **141**, 7955 (2019).

[52] C. Liu, W. Huhn, K.-Z. Du, A. Vazquez-Mayagoitia, D. Dirkes, W. You, Y. Kanai, D. B. Mitzi, and V. Blum, Tunable Semiconductors: Control over Carrier States and Excitations in Layered Hybrid Organic-Inorganic Perovskites, Phys. Rev. Lett. **121**, 146401 (2018).

[53] M. Steger, S. M. Janke, P. C. Sercel, B. W. Larson, H. Lu, X. Qin, V. W.-z. Yu, V. Blum, and J. L. Blackburn, On the optical anisotropy in 2D metal-halide perovskites, Nanoscale **14**, 752 (2022).

[54] S. Kim, M. Lee, C. Hong, Y. Yoon, H. An, D. Lee, W. Jeong, D. Yoo, Y. Kang, Y. Youn, and S. Hang, A band-gap database for semiconducting inorganic materials calculated with hybrid functional, Sci. Data **7**, 387 (2020).

[55] J. P. Perdew, K. Burke, and M. Ernzerhof, Generalized Gradient Approximation Made Simple, Phys. Rev. Lett. **77**, 3865 (1996).

[56] A. Tkatchenko and M. Scheffler, Accurate Molecular van Der Waals Interactions from Ground-State Electron Density and Free-Atom Reference Data, Phys. Rev. Lett. **102**, 073005 (2009).

[57] K.-z. Du, Q. Tu, X. Zhang, Q. Han, J. Liu, S. Zauscher, and D. B. Mitzi, Two-dimensional lead(II) halide-based hybrid perovskites templated by acene alkylamines: Crystal structures, optical properties, and piezoelectricity, Inorg. Chem. **56**, 9291 (2017).

[58] N. E. Wright, X. Qin, J. Xu, L. L. Kelly, S. P. Harvey, M. F. Toney, V. Blum, and A. D. Stiff-Roberts, Influence of annealing and composition on the crystal structure of mixed-halide, Ruddlesden–Popper perovskites, Chem. Mater. **34**, 3109 (2022).

[59] B. Febriansyah, T. M. Koh, Y. Lekina, N. F. Jamaludin, A. Bruno, R. Ganguly, Z. X. Shen, S. G. Mhaisalkar, and J. England, Improved photovoltaic efficiency and amplified photocurrent generation in mesoporous $n = 1$ two-dimensional lead–iodide perovskite solar cells, Chem. Mater. **31**, 890 (2019).

[60] D. B. Straus, N. Iotov, M. R. Gau, Q. Zhao, P. J. Carroll, and C. R. Kagan, Longer cations increase energetic disorder in excitonic 2D hybrid perovskites, J. Phys. Chem. Lett. **10**, 1198 (2019).

[61] K. Shibuya, M. Koshimizu, F. Nishikido, H. Saito, and S. Kishimoto, Poly[bis(phenethylammonium) [dibromidoplumbate(II)]-di-μ-bromido]], Acta Crystallogr. Sec. E **65**, m1323 (2009).

[62] X. Gong, O. Voznyy, A. Jain, W. Liu, R. Sabatini, Z. Piontkowski, G. Walters, G. Bappi, S. Nokhrim, O. Bushuyev *et al.*, Electron–phonon interaction in efficient perovskite blue emitters, Nat. Mater. **17**, 550 (2018).

[63] D. B. Mitzi, K. Chondroudis, and C. R. Kagan, Design, structure, and optical properties of organic−inorganic perovskites containing an oligothiophene chromophore, Inorg. Chem. **38**, 6246 (1999).

[64] M. T. Weller, O. J. Weber, P. F. Henry, A. M. Di Pumpo, and T. C. Hansen, Complete structure and cation orientation in the perovskite photovoltaic methylammonium lead iodide between 100 and 352 K, Chem. Commun. **51**, 4180 (2015).

[65] P. Deák, B. Aradi, T. Frauenheim, E. Janzén, and A. Gali, Accurate defect levels obtained from the HSE06 range-separated hybrid functional, Phys. Rev. B **81**, 153203 (2010).

[66] M. Chagas da Silva, M. Lorke, B. Aradi, M. Farzalipour Tabriz, T. Frauenheim, A. Rubio, D. Rocca, and P. Deák, Self-Consistent Potential Correction for Charged Periodic Systems, Phys. Rev. Lett. **126**, 076401 (2021).

[67] C. Freysoldt, B. Grabowski, T. Hickel, J. Neugebauer, G. Kresse, A. Janotti, and C. G. Van de Walle, First-principles calculations for point defects in solids, Rev. Mod. Phys. **86**, 253 (2014).

[68] T. Gake, Y. Kumagai, C. Freysoldt, and F. Oba, Finite-size corrections for defect-involving vertical transitions in supercell calculations, Phys. Rev. B **101**, 020102 (2020).

[69] Y.-S. Kim, M. Marsman, G. Kresse, F. Tran, and P. Blaha, Towards efficient band structure and effective mass calculations for III-V direct band-gap semiconductors, Phys. Rev. B **82**, 205212 (2010).

[70] A. Goyal, S. McKechnie, D. Pashov, W. Tumas, M. van Schilfgaarde, and V. Stevanović, Origin of pronounced nonlinear band gap behavior in lead–tin hybrid perovskite alloys, Chem. Mater. **30**, 3920 (2018).

[71] L. Mao, H. Tsai, W. Nie, L. Ma, J. Im, C. C. Stoumpos, C. D. Malliakas, F. Hao, M. R. Wasielewski, A. D. Mohite, and M. G. Kanatzidis, Role of organic counterion in lead- and tin-based two-dimensional semiconducting iodide perovskites and application in planar solar cells, Chem. Mater. **28**, 7781 (2016).

[72] J. Li, Q. Yu, Y. He, C. C. Stoumpos, G. Niu, G. G. Trimarchi, H. Guo, G. Dong, D. Wang, L. Wang, and M. G. Kanatzidis, $Cs_2PbI_2Cl_2$, All-inorganic two-dimensional Ruddlesden–Popper mixed halide perovskite with optoelectronic response, J. Am. Chem. Soc. **140**, 11085 (2018).

[73] Y.-Q. Zhao, Q.-R. Ma, B. Liu, Z.-L. Yu, J. Yang, and M.-Q. Cai, Layer-dependent transport and optoelectronic property in two-dimensional perovskite: $(PEA)_2PbI_4$, Nanoscale **10**, 8677 (2018).

[74] M. L. Tietze, P. Pahner, K. Schmidt, K. Leo, and B. Lüssem, Doped organic semiconductors: Trap-filling, impurity saturation, and reserve regimes, Adv. Funct. Mater. **25**, 2701 (2015).

[75] S. Heo, G. Seo, Y. Lee, D. Lee, M. Seol, J. Lee, J.-B. Park, K. Kim, D.-J. Yun, Y. S. Kim *et al*, Deep level trapped defect analysis in $CH_3NH_3PbI_3$ perovskite solar cells by deep level transient spectroscopy, Energy Environ. Sci. **10**, 1128 (2017).

[76] A. R. Srimath Kandada and C. Silva, Exciton polarons in two-dimensional hybrid metal-halide perovskites, J. Phys. Chem. Lett. **11**, 3173 (2020).

[77] R. Wang, X. Zhang, J. He, C. Ma, L. Xu, P. Sheng, and F. Huang, Bi^{3+}-doped $CH_3NH_3PbI_3$: Red-shifting absorption edge and longer charge carrier lifetime, J. Alloys Compd. **695**, 555 (2017).

[78] J. A. Kohn, Contamination of the characteristic *x*-radiation of copper by Fe, Cr and Ni radiation, Am. Mineral. **41**, 514 (1956).

[79] G. Sheldrick, Crystal structure refinement with SHELXL, Acta Crystallogr. Sec. C **71**, 3 (2015).

[80] O. V. Dolomanov, L. J. Bourhis, R. J. Gildea, J. A. K. Howard, and H. Puschmann, OLEX2: A complete structure solution, refinement and analysis program, J. Appl. Crystallogr. **42**, 339 (2009).

[81] G. Kortüm, W. Braun, and G. Herzog, Principles and techniques of diffuse-reflectance spectroscopy, Angew. Chem., Int. Ed. **2**, 333 (1963).

[82] J. Heyd, G. E. Scuseria, and M. Ernzerhof, Hybrid functionals based on a screened Coulomb potential, J. Chem. Phys. **118**, 8207 (2003).

[83] J. Heyd, G. E. Scuseria, and M. Ernzerhof, Erratum: "Hybrid functionals based on a screened Coulomb potential" [J. Chem. Phys. 118, 8207 (2003)], J. Chem. Phys. **124**, 219906 (2006).